Research Square

Preprints are preliminary reports that have not undergone peer review.
They should not be considered conclusive, used to inform clinical practice,
or referenced by the media as validated information.

Metastable Hexagonal Close-Packed Palladium Hydride in Liquid Cell Transmission Electron Microscopy

Dong Won Chun (chundream98@kist.re.kr)
Korea Institute of Science and Technology https://orcid.org/0000-0001-8813-5134
Jaeyoung Hong
Korea Institute of Science and Technology
Jee-Hwan Bae
Korea Institute of Science and Technology https://orcid.org/0000-0003-3417-4351
Hyesung Jo
Korea Advanced Institute of Science and Technology
Hee-Young Park
Korea Institute of Science and Technology
Sehyun Lee
Korea Institute of Science and Technology
Sung Jun Hong
Yonsei University
Hoje Chun
Yonsei University
Min Kyung Cho
Korea Institute of Science and Technology
Juyoung Kim
Korea Institute of Science and Technology
Joodeok Kim
Seoul National University
Yongju Son
Seoul National University
Haneul Jin
Korea Institute of Science and Technology
Jin-yoo Suh
Korea Institute of Science and Technology
Sung-Chul Kim
Korea Institute of Science and Technology https://orcid.org/0000-0003-0512-1154
Ha-Kyung Roh

Korea Institute of Science and Technology

Kyu Hyoung Lee
Yonsei University https://orcid.org/0000-0001-6843-6706

Hyung-Seok Kim
Korea Institute of Science and Technology

Kyung Yoon Chung
Korea Institute of Science and Technology https://orcid.org/0000-0002-1273-746X

Chang Won Yoon
Korea Institute of Science and Technology

Kiryeong Lee
Korea Institute of Science and Technology

Seo Hee Kim
Korea Institute of Science and Technology

Jae-Pyoung Ahn
Korea Institute of Science and Technology https://orcid.org/0000-0003-2657-7425

Hionsuck Baik
Korea Basic Science Institute

Gyeung Ho Kim
Korea Institute of Science and Technology

Byungchan Han
Yonsei University https://orcid.org/0000-0002-2325-6733

Sungho Jin
University of California San Diego

Taeghwan Hyeon
Seoul National University https://orcid.org/0000-0001-5959-6257

Jungwon Park
Seoul National University https://orcid.org/0000-0003-2927-4331

Chang Yun Son
Pohang University of Science and Technology

Yongsoo Yang
Korea Advanced Institute of Science and Technology (KAIST) https://orcid.org/0000-0001-8654-302X

Young-Su Lee
Center for Energy Materials Research, Korea Institute of Science and Technology

Sung Jong Yoo
Korea Institute of Science and Technology https://orcid.org/0000-0003-0238-5971

Physical Sciences - Article

Keywords: Metastable Phases, Rational Design and Synthesis, Monte Carlo Simulation, Liquid Cell TEM, Atomic Electron Tomography, Metastability-engineering Strategy

Posted Date: December 14th, 2020

DOI: https://doi.org/10.21203/rs.3.rs-104262/v1

License: This work is licensed under a Creative Commons Attribution 4.0 International License.
Read Full License

Version of Record: A version of this preprint was published at Nature on March 23rd, 2022. See the published version at https://doi.org/10.1038/s41586-021-04391-5.

Abstract

Metastable phases—kinetically favored structures—are ubiquitous in nature. Rather than forming thermodynamically stable ground-state structures, crystals grown from high-energy precursors often initially adopt metastable structures depending on the initial conditions such as temperature, pressure, or crystal size. As the crystals grow further, they typically undergo a series of transformations from metastable to lower-energy phases and ultimately energetically stable phases, as described by Wilhelm Ostwald. Metastable phases, however, sometimes provide superior chemical and physical properties, and hence, discovering and synthesizing novel metastable phases are promising avenues for achieving innovations in materials science. The most common strategy for synthesizing a metastable material involves manipulating thermodynamic conditions such as temperature and pressure during the course of synthesis. However, the search for metastable materials has mainly been heuristic, on the basis of experiences, intuitions, or even speculative predictions. This limitation necessitates the advent of a new paradigm to discover novel metastable phases, i.e., by “rational design and synthesis” instead of a “rule of thumb,” and based on ab initio methods, i.e., the calculation of thermodynamic and kinetic properties of materials with various compositions, crystal structures, and crystal sizes. The design rule is embodied in the discovery of a metastable hexagonal close-packed (HCP) palladium hydride (PdH_x), synthesized in a liquid cell environment using a transmission electron microscope (TEM). The metastable HCP structure is stabilized through a unique interplay among the precursor concentrations in the solution: a sufficient supply of hydrogen (H) favors the HCP structure on the sub-nanometer scale, and an insufficient supply of Pd inhibits further growth and subsequent transition toward the thermodynamically stable face-centered cubic (FCC) structure. The crystal structure was modulated (HCP or FCC) by adjusting the H concentration inside the TEM liquid cell, providing strong evidence for the crucial role of the H concentration. Monte Carlo simulations reveal that an unexpected inhomogeneous distribution of interstitial H atoms, distinct from the predominant occupation at the octahedral interstitial sites, is key to stabilizing nanoscale HCP PdH_x. Furthermore, insufficient Pd brings a multi-step nucleation and growth pathway, deduced from in situ liquid cell TEM combined with atomic electron tomography, which maintains the metastable phase intact. These findings provide new thermodynamic insights into metastability-engineering strategy to be deployed in discovering new metastable phases.

Main Text

The advent of liquid cell transmission electron microscopy (TEM) enables the direct imaging and growth of materials in liquids. The electron beam generated inside the microscope transfers high energy to the irradiated suspending liquid; water molecules decompose into radicals and molecules including hydrated electrons (e_h^-), hydroxyl radicals ($OH^\cdot$), hydrogen radicals ($H^\cdot$), and hydrogen molecules (H_2). This radiation chemistry of water results in distinct phenomena in liquid cell TEM. Examples include nanocrystal growth via the reaction of precursors and e_h^-, the most reactive radiolysis product, and bubbles formed by a high H_2 concentration.

Face-centered cubic (FCC) palladium hydride (PdH_x) constitutes the most important model system for fundamental studies of H in metals[6,7]. Generally, the PdH_x phase can form upon the adsorption and dissociation of H_2 on the Pd surface followed by surface, subsurface, and interstitial site occupations of hydrogen atoms[6]. Similar to metallic Pd, the PdH_x phase has a FCC structure, where the octahedral (O) interstitial sites are occupied by H atoms, providing two distinct phases: a low-H-concentration a-phase and a high-H-concentration b-phase (x £ 0.7)[6].

In this study, we synthesized metastable hexagonal close-packed (HCP) PdH_x nanoparticles via liquid-cell TEM by employing a graphene liquid cell (GLC)[8]. Specifically, a Pd precursor solution was encapsulated between two multilayer graphene layers, and e_h^- produced by the electron beam initiated the nucleation and growth of nanoparticles (Movies S1 and S2)[9], as observed by TEM (Methods). Owing to the free rotation of the nanoparticles in the liquid[10], diffraction patterns (DPs) with distinct zone axes can be acquired to determine their crystal structures.

Remarkably, DPs obtained from in situ TEM (Figs. 1a, b) and ex situ high-resolution scanning transmission electron microscopy (HR-STEM) (Fig. 1e, Methods) images of the synthesized nanoparticles corresponded to an HCP lattice rather than an FCC lattice, the structure of almost every Pd compound ever reported[11-13], regardless of its growth pathway, i.e., monomer attachment (particle 1, Figs. 1a, c) or coalescence (particle 2, Figs. 1b, d). Notably, no phase transformation from FCC to HCP was observed: the particles having HCP structures were HCP from the beginning. The interplanar distance values of low-index planes remained almost unchanged during growth, showing the rigidity of the structure (Figs. 1c, d). The ABAB stacking, a distinctive characteristic of HCP phases, was clearly revealed in the HR-STEM image (Fig. 1f).

The statistical analysis of lattice constants derived from the DPs (Methods) revealed that the HCP nanoparticles expanded in volume (~23%) with respect to the ideal HCP Pd lattice according to density functional theory (DFT) calculations (Fig. 1g, Extended Data Table 1), implying that the produced nanoparticles were more likely a Pd compound than pure Pd. Furthermore, the energy dispersive X-ray spectroscopy (EDS) and electron energy loss spectroscopy (EELS) results (Fig. 1h, Extended Data Fig. 1) suggest that PdH_x formed.

The stabilities of PdH_x (0 £ x £ 1) in FCC and HCP structures were examined by DFT calculations and Monte Carlo (MC) simulations using the embedded atom method (EAM) potential model[14] (Methods). As expected, the total energy of the bulk periodic PdH_x crystals estimated from both DFT and MC calculations predicted the FCC structure to be more stable than the HCP structure for all values of x, with the H atoms in PdH_x preferring to occupy the octahedral interstitial sites, regardless of the crystal packing (Fig. 2a). Therefore, the simulation results regarding the ideal bulk PdH_x do not support the formation of HCP nanoparticles.

Surprisingly, MC simulations with various particle sizes revealed that HCP PdH is more stable than FCC PdH for nanocrystals with diameters of less than 2 nm (Figs. 2b, c). The occupancy of H atoms mainly depends on the size as well as the crystal packing (Extended Data Fig. 2); the large fraction of surface Pd atoms having incomplete secondary coordination results in irregular size-dependencies. Consequently, the extra stabilization for O sites introduced by 1-4 layers overlap (ABCA') in FCC Pd is significantly reduced for the small particles that only accommodate five layers of Pd atoms (Fig. 2e, Extended Data Fig. 2g). In contrast, the stability of O sites in the HCP Pd nanoparticle would not be affected by the presence of a small number of layers, as no Pd atoms vertically overlap with the O sites in HCP stacking (Fig. 2f, Extended Data Fig. 2h). Interestingly, HCP packing is preferred at higher H contents ($x > 0.6$, Fig. 2c), mainly due to the difference in the surface H atom fraction between high ($x = 1$, Extended Data Fig. 2a) and low ($x = 0.2$, Extended Data Fig. 2d) H concentrations, which implies that the sufficient H supply in the liquid cell participates in the nucleation and growth and facilitates the formation of HCP PdH_x.

To verify the MC-derived formation mechanism of HCP PdH_x, we synthesized PdH_x nanoparticles by modulating the H concentration via tuning the electron dose rate (EDR) and adopting a different liquid cell system for TEM, a Si_3N_4 liquid cell (SLC) (Fig. 3). These experiments suggest three distinctive trends.

First, all of the observed nanoparticles exhibit the HCP structure at high EDRs ($> 5 \times 10^3$ $e^-/Å^2s$) in both liquid cells (Figs. 3a, b), which indicates the effect of pressure in GLC due to van der Waals forces[15,16] and the preferential formation of the HCP structure by epitaxial growth on top of the hexagonal graphene window material[17] can be excluded.

Second, at low EDR ($< 5 \times 10^2$ $e^-/Å^2s$), both FCC (~30%) and HCP (~70%) particles were observed in GLC (Fig. 3c), whereas 100% of the nanoparticles observed in SLC were FCC (Fig. 3d), implying that the H concentration plays a crucial role in HCP formation, as suggested by MC simulations. The production of FCC particles around hydrogen bubbles (which form when the radiolysis products exceed their critical concentration[9]) in GLC under the higher EDR is another piece of evidence for the key role of H in the formation of the HCP structure (Extended Data Figs. 3a, b). These bubbles remove supersaturated H, resulting in a condition favoring the formation of FCC PdH_x.

The distinction between GLC and SLC may have been due to their different electron absorption rates (EARs), which are in turn due to their different components with different thicknesses, namely, graphene (~1 nm) and Si_3N_4 (50 nm) windows. The measurement of the transmitted electron intensity indicated an approximately 10% lower EAR for the GLC than that for the SLC, which can result in a higher H concentration that facilitates the formation of HCP. In addition, Pd atoms adsorbed on the graphene surface can promote the production of atomic H and catalyze Pd–H bonding, further facilitating the formation of HCP PdH_x in GLC[18].

Third, the unit cell volumes of the HCP PdH_x nanoparticles at high EDRs were greater than those of the HCP nanoparticles at low EDRs, presumably owing to the higher H concentration (Figs. 3e–g). The H

content x in HCP PdH_x was estimated by comparing the volume per Pd atom derived from TEM with that from the DFT calculations (Extended Data Fig. 4a). The approximate H content increases with EDR and approaches x ~ 1 at a high EDR, suggesting equivalenced PdH formation. In contrast, the maximum estimated H content in FCC nanoparticles at a low EDR is x ~ 0.2 (Extended Data Fig. 4b).

We also produced nanoparticles without using the TEM by instead employing a newly designed system for electron-beam-induced synthesis (Extended Data Figs. 3c–e, Methods). All of these particles exhibited an FCC structure with lattice constants slightly larger than those of the standard FCC Pd (Extended Data Fig. 3d), with an x value of only approximately 0.002, which may have been due to a low H supply as a consequence of low EDRs. With this information in hand, we conclude that the HCP PdH_x formation process is highly dependent on the anomalous H supply originating from radiolysis.

An abundant supply of H may also modulate the growth kinetics. According to DFT-calculations, adding another layer of Pd onto the (111) surface of FCC PdH requires more energy than adding onto the (0001) surface of HCP PdH. This higher energy cost is compensated by a more exothermic reaction with H atoms in the FCC structure (Extended Data Fig. 5). This result can be interpreted as the passivation of FCC PdH particles by H radicals, which in turn stabilizes the surface and disfavors the further incorporation of Pd, resulting in slower growth. In addition, more rapidly growing HCP particles would quickly deplete the Pd precursors, further suppressing the growth of FCC particles.

As a metastable solid phase initially forms, it dissolves and is replaced by a more stable phase via several thermodynamically permissible pathways until the most stable phase is formed, as described by Wilhelm Ostwald[3]. Hence, a remaining question is how an HCP nanoparticle maintains its crystal structure instead of transforming into FCC, even when it enters a size regime that is unstable for HCP as it grows. Generally, the synthesis of a nanocrystal in an aqueous solution is based on there being a sufficient supply of precursors to facilitate the formation of a thermodynamically stable phase.

In contrast, in liquid cell TEM, the initially grown metastable phases form a region of supersaturated precursors with much higher concentrations than those of these precursors in the as-made solutions[19]; at the same time, the initially grown metastable phases are rapidly depleting the precursors in the surrounding area[20], a process that can delay further growth and transformation into the stable phase, eventually leaving the metastable phase intact. We heated PdH_x nanoparticle at 500 °C for 2 h in an in situ heating system (Methods, Extended Data Fig. 6) to induce phase transformation. Remarkably, the HCP nanoparticle held its structure after annealing, indicating that HCP PdH_x is indeed a metastable phase and that the energy barrier between this phase and the stable phase is quite high.

To gain deeper insights into the growth mechanism of HCP PdH_x, the detailed three-dimensional (3D) atomic arrangement of a PdH_x nanoparticle was investigated by performing atomic electron tomography (AET)[21-23]. A STEM tomography dataset was acquired at 33 different tilt angles ranging from –70° to 70°, and an atomic-resolution 3D tomogram was obtained using the GENFIRE algorithm (Methods)[24]. Individual atoms were clearly resolved in the reconstruction as local intensity maxima (Figs. 4a–c). The

full 3D coordinates of individual atoms were traced by 3D Gaussian fitting at each local maximum, resulting in a 3D atomic model of the nanoparticle (Methods). To verify whether the nanoparticle indeed forms an HCP structure, local hexagonal stacking types were determined for each atom. As shown in Fig. 4d, each atom in an HCP crystal can have two different types of nearest neighbor arrangements, namely, type A and type B. A perfect HCP crystal is expected to show alternating layers of type-A and type-B atoms. Interestingly, the measured nanoparticle was not a perfect HCP single crystal, but it exhibited a complex domain structure with different regions of ABAB and BABA stacking, as shown in Figs. 4a–c, e. Nevertheless, the 3D connectivity of these different types of domains (blue and red regions in Fig. 4e, exhibiting ABAB or BABA stacking, respectively) and their excellent agreement with the ideal HCP structure (Extended Data Fig. 7a) suggested that the nanoparticle indeed possessed HCP ordering.

Remarkably, the boundary between the two anti-phase HCP stacking domains (Fig. 4e) appears to be severely indented and irregularly shaped. This observation cannot be easily explained by coalescence events (aggregation or oriented attachment) because they usually result in sharp planar boundaries[8,10,25-27]. Instead, the presence of a complex boundary structure (Fig. 4f) suggests that the nanoparticle probably formed as a result of a multi-step crystallization process that is more energetically favorable than direct crystallization[28-30], as described in Extended Data Fig. 8h. Note that no diffraction peaks were observed at the early stage of growth (< ~1 s), indicating an amorphous phase, which further supports the multi-step crystallization mechanism (Extended Data Figs. 8a–g).

The stabilization of the sub-nanometer-sized particles of HCP PdH predicted by MC simulations corroborates the multi-step crystallization process suggested by the AET experiment. Overall, the experimentally resolved atomic structure shows a domain size of approximately 1–2 nm (Extended Data Fig. 7a), similar to the nucleus diameter of 1.2 nm that favors the formation of HCP PdH (Figs. 2b–c). The transition to HCP crystal nuclei from the amorphous phase and subsequent growth of the crystalline parts via merging enables the formation of multi-domain HCP PdH nanoparticles, which can grow larger than about a nanometer, the size limit for HCP PdH single crystals being more stable than FCC PdH.

In this study, we discovered a new metastable HCP PdH_x for the first time. The unique environment in the liquid cell—namely, the limited quantity of Pd precursors and continuous supply of H—results in the formation of the HCP phase owing to the nonuniform H distribution, and the transformation to the stable FCC phase was inhibited because of the multi-step growth pathway. The metastable HCP PdH_x exhibited a superior H capacity and stronger H binding compared with its FCC counterpart. This insight may provide a new route for designing and synthesizing novel energy storage materials. For example, in contrast with the conventional fabrication procedure based on a phase transformation driven by intercalation and dissolution, the procedure involving synthesizing materials for H storage or Li-ion battery electrodes under a high concentration of H or Li could result in a new metastable phase. Such synthesis of novel metastable phases by the proposed approach will be pursued in future work.

References

1 Sun, W. *et al.* The thermodynamic scale of inorganic crystalline metastability. *Sci. Adv.* **2**, e1600225 (2016).

2 Martinolich, A. J. & Neilson, J. R. Toward reaction-by-design: achieving kinetic control of solid state chemistry with metathesis. *Chem. Mater.* **29**, 479-489 (2017).

3 Gopalakrishnan, J. Chimie douce approaches to the synthesis of metastable oxide materials. *Chem. Mater.* **7**, 1265-1275 (1995).

4 Chen, B.-R. *et al.* Understanding crystallization pathways leading to manganese oxide polymorph formation. *Nat. Commun.* **9**, 2553 (2018).

5 Aykol, M., Dwaraknath, S. S., Sun, W. & Persson, K. A. Thermodynamic limit for synthesis of metastable inorganic materials. *Sci. Adv.* **4**, eaaq0148 (2018).

6 Baldi, A., Narayan, T. C., Koh, A. L. & Dionne, J. A. In situ detection of hydrogen-induced phase transitions in individual palladium nanocrystals. *Nat. Mater.* **13**, 1143-1148 (2014).

7 Griessen, R., Strohfeldt, N. & Giessen, H. Thermodynamics of the hybrid interaction of hydrogen with palladium nanoparticles. *Nat. Mater.* **15**, 311-317 (2016).

8 Yuk, J. M. *et al.* High-resolution EM of colloidal nanocrystal growth using graphene liquid cells. *Science* **336**, 61-64 (2012).

9 Schneider, N. M. *et al.* Electron–water interactions and implications for liquid cell electron microscopy. *J. Phys. Chem. C* **118**, 22373-22382 (2014).

10 Park, J. *et al.* 3D structure of individual nanocrystals in solution by electron microscopy. *Science* **349**, 290-295 (2015).

11 Sachs, C. *et al.* Solubility of hydrogen in single-sized palladium clusters. *Phys. Rev. B* **64**, 075408 (2001).

12 Moore Jr, W. J. & Pauling, L. The crystal structures of the tetragonal monoxides of lead, tin, palladium, and platinum. *J. Am. Chem. Soc.* **63**, 1392-1394 (1941).

13 Cadeville, M. & Lerner, C. On the electronic structure of interstitial transition-metal based alloys with boron and carbon impurities: Part I. Experimental study. *Philos. Mag.* **33**, 801-824 (1976).

14 Zhou, X., Zimmerman, J. A., Wong, B. M. & Hoyt, J. J. An embedded-atom method interatomic potential for Pd–H alloys. *J. Mater. Res.* **23**, 704-718 (2008).

15 Algara-Siller, G. *et al.* Square ice in graphene nanocapillaries. *Nature* **519**, 443-445 (2015).

16 Yang, X., Li, H., Ahuja, R., Kang, T. & Luo, W. Formation and electronic properties of palladium hydrides and palladium-rhodium dihydride alloys under pressure. *Sci. Rep.* **7**, 3520 (2017).

17 Walter, J., Heiermann, J., Dyker, G., Hara, S. & Shioyama, H. Hexagonal or quasi two-dimensional palladium nanoparticles—tested at the Heck reaction. *J. Catal.* **189**, 449-455 (2000).

18 López-Corral, I., Germán, E. a., Juan, A., Volpe, M. a. A. & Brizuela, G. P. DFT study of hydrogen adsorption on palladium decorated graphene. *J. Phys. Chem. C* **115**, 4315-4323 (2011).

19 Loh, N. D. *et al.* Multistep nucleation of nanocrystals in aqueous solution. *Nat. Chem.* **9**, 77-82 (2017).

20 Nielsen, M. H., Aloni, S. & De Yoreo, J. J. In situ TEM imaging of $CaCO_3$ nucleation reveals coexistence of direct and indirect pathways. *Science* **345**, 1158-1162 (2014).

21 Dabov, K., Foi, A., Katkovnik, V. & Egiazarian, K. Image denoising by sparse 3-D transform-domain collaborative filtering. *IEEE Trans. Image Process.* **16**, 2080-2095 (2007).

22 Xu, R. *et al.* Three-dimensional coordinates of individual atoms in materials revealed by electron tomography. *Nat. Mater.* **14**, 1099-1103 (2015).

23 Yang, Y. S. *et al.* Deciphering chemical order/disorder and material properties at the single-atom level. *Nature* **542**, 75-79 (2017).

24 Zhou, J. H. *et al.* Observing crystal nucleation in four dimensions using atomic electron tomography. *Nature* **570**, 500-503 (2019).

25 Kim, B. H. *et al.* Critical differences in 3D atomic structure of individual ligand-protected nanocrystals in solution. *Science* **368**, 60-67 (2020).

26 Li, D. *et al.* Direction-specific interactions control crystal growth by oriented attachment. *Science* **336**, 1014-1018 (2012).

27 Lange, A. P. *et al.* Dislocation mediated alignment during metal nanoparticle coalescence. *Acta Mater.* **120**, 364-378 (2016).

28 Zhang, T. H. & Liu, X. Y. How does a transient amorphous precursor template crystallization. *J. Am. Chem. Soc.* **129**, 13520-13526 (2007).

29 Lee, J., Yang, J., Kwon, S. G. & Hyeon, T. Nonclassical nucleation and growth of inorganic nanoparticles. *Nat. Rev. Mater.* **1**, 16034 (2016).

30 Guo, C., Wang, J., Li, J., Wang, Z. & Tang, S. Kinetic pathways and mechanisms of two-step nucleation in crystallization. *J. Phys. Chem. Lett.* **7**, 5008-5014 (2016).

Methods

Precursor solution. The palladium precursor solution was prepared by dissolving sodium tetrachloropalladate(II) (Na_2PdCl_4, Aldrich) and isopropyl alcohol (Junsei) in distilled water[31]. The Pd concentration varied from 3.67 mM to 18 mM, but it did not affect the phase and molar volume of nucleated particles. Most experiments were performed with a 3.67 mM precursor solution. Isopropanol was used as a hydroxyl radical scavenger to minimize the probability of dissolving palladium nanoparticles. The molar concentration of isopropanol in the aqueous solution was 0.1 M[9,32].

Liquid TEM cell. The graphene liquid cell (GLC) was fabricated following the previous reports[8]. Multilayer graphene, which was purchased from Graphene Square Incorporation, was adopted to increase durability of GLC under bombardment of electrons accelerated at a few hundred kilovolts. Silicon nitride liquid cell (SLC) experiments were conducted with a commercial in situ liquid holder, Protochips Poseidon 210, the window of which was 50 nm thick.

TEM. Electron-beam-induced PdH_x nanoparticle growth in liquid was traced in real time with a Titan TEM (FEI Titan 80-300) operated at 300 kV, which was equipped with a OneView CCD camera (Gatan) and a monochromator. We used this TEM to irradiate electrons on a liquid cell to generate particles for ex situ analysis, which was conducted after fully drying the liquid, i.e. by irradiating the liquid in the GLC for ~30 min or exposing the disassembled SLC to vacuum for 48 h. HR-TEM and HR-STEM images as well as raw images for AET of the particles generated in GLC under a high electron dose rate were acquired with a double Cs-corrected Titan Themis TEM (FEI) operated at 300 kV. HR-TEM images of the particles generated at lower dose rates or in SLCs were obtained using the aforementioned Titan TEM.

Monochromated electron energy loss (EEL) spectra of the HCP particles formed inside the SLC were acquired using the Titan TEM operated at 80 kV[6,33]. Energy dispersive X-ray spectroscopy (EDS) analysis was conducted with a Talos TEM (FEI Talos F200X) operated at 200 kV, equipped with a Super-X EDS system that utilizes four silicon drift detectors (SDD).

XRD. X-ray diffraction (XRD) analysis was performed at room temperature in the 2θ range of 10–90° on a D8 Advance (Bruker AXS, Germany) diffractometer equipped with a LynxEye line detector using Cu-Kα radiation (λ = 1.5418 Å) at 40 kV and 40 mA and a scanning rate of 0.5 °/min with a step size of 0.02°.

In order to prove that the lattice of Pd/C was expanded relative to that of pristine Pd, an internal standard of Si powder (NIST SRM 640e) was used. The lattice parameters of Pd/C were refined with the Le Bail

method[34] using TOPAS software (Bruker AXS, Germany)[35]; the lattice parameter of Si was fixed to a = 5.431179 Å.

Lattice constant calculation. The lattice constants of the nanoparticles were calculated from the diffraction patterns of the HR-TEM and HR-STEM images of nanoparticles along the [1-21-3] and [-2110] zone axes. We used the crystallographic relationship formula of the HCP structure below to derive the lattice constants[36].

$$\frac{1}{d_{hkl}^2} = \frac{4}{3}\left(\frac{h^2 + hk + k^2}{a^2}\right) + \frac{l^2}{c^2}$$

The lattice constant a was directly calculated from the (1-100) planes, and the lattice constant c was calculated from the (1-101) planes and the aforementioned (1-100) planes for the particle along the [1-21-3] zone axis. As for the particle along the [-2110] zone axis, the lattice constants a and c were directly calculated from the (0-110) and (0002) planes, respectively. Notably, some particles had quite different lattice constants from the majority of particles. Specifically, some particles had far higher c values, while others had far lower values. These differences were attributed to the deviation in the number of H atoms residing in the particles. As the HCP palladium hydride nanoparticles formed explosively, some particles might have been formed in out-of-average surroundings, i.e., some might have been exposed to an excess of H radicals, while others might have not.

In situ d-spacing tracking. The plane index of diffraction spot, and corresponding d-spacing, acquired when the particle was aligned along the zone axis was obvious, as plane information is manifested in the zone axis pattern. When the particle was not along the zone axis, the diffraction spot of the particle was assigned to a plane index considering the continuity of fringes, and the degree of proximity between the aforementioned d-spacing value in the video and average interplanar distance measured ex situ.

Bulk scale PdH_x/C preparation through e-beam irradiation. To synthesize PdH_x nanoparticles via irradiation with an electron beam in a batch reactor outside TEM, 1 L of 3.67 mM Na_2PdCl_4 in a 0.1 M isopropyl alcohol aqueous solution was prepared. Then, carbon black was added to the reaction solution, which was homogeneously mixed under ultrasonication for 10 min at room temperature. Thereafter, the reaction vessel was placed under electron beam irradiation at a dose rate of 1.9×10^{-3} $e^-/Å^2s$ for several minutes. The resulting solution was filtered with distilled water several times, and black precipitates were obtained.

Data acquisition. A tomographic tilt series of a PdH_x nanoparticle was obtained using the Titan Themis TEM. In HAADF-STEM mode, 33 tilt series images of 1,024 × 1,024 pixels were obtained between -70.0° and +70.0° with a 35.50 pm pixel size. Ten images were consecutively acquired for each tilt angle with a 3 μs dwell time. A linear drift constant was estimated from consecutive images and corrected for each angle. Then, scan distortion correction was applied to correct the image distortions owing to slight misalignment between the x and y directions of the scan coil, based on a reference image of the Si (110) zone axis taken under the same measurement conditions.

Image denoising. HAADF-STEM images suffer from Poisson–Gaussian noise. The Poisson and Gaussian noise parameters were estimated from the image statistics of the ten consecutively acquired images, and a sparsity-based transform domain denoising (BM3D) was applied, as described in Refs. 10–14.[21-24,37]

GENFIRE reconstruction. After denoising, the projections were aligned based on the common line and center of mass methods for alignment along the tilt axis direction and perpendicular to the tilt axis direction, respectively[23,24,37-39]. Tomographic reconstruction was performed using GENFIRE for the aligned tilt-series images[23,24,37-40] with an oversampling ratio of 4 and interpolation radius of 0.1 pixel. To improve the quality of the reconstruction, an angular refinement process was applied to minimize the discrepancy between the forward-projected projections of the reconstruction volume and the experimental projections[40]. The final reconstruction obtained after the refinement process showed a clear atomic-resolution internal structure.

3D identification of atomic coordinates (tracing). The 3D atomic coordinates of all atoms in the nanoparticle were determined by fitting a 3D Gaussian function on a 5 × 5 × 5 voxel volume near each local maximum. The fittings were performed in descending order from the highest intensity local maximum, and a minimum distance constraint of 2.4 Å was enforced during the process. However, owing to the atom elongation effect resulting from the missing wedge and slight imperfectness of the reconstruction, several connected intensity blobs were not properly traced owing to the failure to properly identify the local maxima. To locate the untraced atoms, the reconstruction volume was sliced along the hexagonal c axis at each atomic layer, and the local maxima in each slice were identified. Then, the same Gaussian fitting procedure was repeated using the new local maxima in descending order, still enforcing the same minimum distance constraint. After this process, a final 3D atomic model of 9,868 atoms was obtained.

Assignment of HCP lattice sites. To analyze the 3D atomic structure, proper HCP lattice sites must be assigned for each atom. To begin the assignment procedure, the HCP lattice vectors for the nanoparticle were roughly estimated from the peak positions in the 3D Fourier transformed reconstruction volume. Then, an atom closest to the mean position of the given 3D atomic coordinates was selected. The first selected atom was assigned to the origin of the HCP lattice. From the starting atom, the positions of the 12 nearest neighbor (n.n.) atoms and corresponding n.n. HCP lattice sites were calculated. At each n.n. position, a sphere was drawn with a radius of ¼ n.n. distance. If an atom was encompassed by the sphere, the atom was assigned to the lattice site corresponding to the n.n. position. This process was continued for all newly assigned HCP lattice sites and repeated until there were no newly assigned sites. Note that an atom in an HCP structure can have two different types of n.n. structure, as described in Fig. 4d. To determine which n.n. structure the starting atom belonged to, the process above was repeated twice for two different n.n. structures, and the one that resulted in a larger number of assigned HCP sites was chosen. After assigning HCP lattice sites for all available atoms, the HCP lattice vectors were fitted to minimize the error between the measured atomic positions and the corresponding lattice positions of the fitted HCP lattice. The entire process described above was continuously repeated with the newly obtained HCP lattice vectors until there the lattice vectors stopped changing.

Domain identification. For the initial trial, HCP lattice assignment and lattice parameter fitting were performed assuming that the entire nanoparticle is an HCP single crystal, resulting in initial HCP lattice vectors. However, the nanoparticle is not guaranteed to form a single crystal. Therefore, local lattice assignments and fittings described above were individually performed for all the atoms within the nanoparticle to check their n.n. ordering. For the local fitting, only the atoms within the distance of the mean of n.n. and next-nearest-neighbor (n.n.n.) distance, which was determined from the HCP fitting of the entire nanoparticle, were used. From the local fittings, the local lattice constant and n.n. structure type (Fig. 4d, named as type A or type B here) can be obtained for each atom. After the local fitting, all the atoms were assigned to the closest atomic layer perpendicular to the hexagonal c axis (Fig. 4e). Then, type-A atoms in odd-numbered layers and type-B atoms in even numbered layers were classified as ABAB stacking, and the opposite cases were classified as BABA stacking. As shown in Fig. 4e, atoms with the same stacking type form clusters.

To identify the connected clusters, we performed a local connectivity analysis. First, we selected a starting atom, around which we drew a sphere, with the mean of the n.n. and n.n.n. distance for the radius. Then, among the atoms within the sphere, we counted how many atoms share the same stacking type with the selected atom. If the number was larger than a certain threshold, the selected atom was considered to be within a connected domain, and a specific domain identifier was assigned to it. In this case, we added atoms with the same stacking type as the selected atom to the potential domain atom list, and we repeated the process for all the newly added atoms in the list. For all the atoms that fulfilled the number threshold, the same domain identifier was assigned. For atoms which could not meet the number threshold, we checked whether all of the atoms in their local sphere had the same atom type. If

that was the case, we assigned the same domain identifier to the atom. Otherwise, the atom was marked as a non-domain atom (not belonging to any domain). We repeated the procedure above until there were no newly added atoms in the potential domain atom list. Finally, a collection of atoms with the same domain identifier could be identified, which formed a domain. We repeated this entire process with each other atom as a starting atom with a different domain identifier. After running the process through all available atoms, all connected domains in the nanoparticle could be identified. Individual HCP lattices could be separately assigned and fitted to each identified domain to correctly determine their lattice constants.

We tested several different number thresholds for this analysis, and using a number threshold of 7 yielded the largest number of atoms successfully assigned to HCP lattice sites after separate domain fittings. Using this threshold, we found five connected domains in the nanoparticle, which contained 3,392, 3,552, 9, 7, and 2 atoms. The remaining 2,906 atoms were not assigned to any domain. Finally, the HCP lattice constants of a = 2.9539 Å and c = 4.6692 Å were obtained by averaging each domain's lattice constants weighted by the number of atoms.

DFT calculations. The stability of FCC PdH_x and HCP PdH_x was compared using density functional theory (DFT) calculations, which were carried out using the Quantum-ESPRESSO package[41,42] with PBEsol[43] as an exchange-correlation functional and the projector augmented wave[44] pseudopotentials generated by the atomic code[45]. The PBEsol functional was employed because it accurately reproduces the experimental lattice parameters of PdH[46], which is important in the current study. The planewave cut-off energy was set to 60 Ry. We performed phonon calculations within the density functional perturbation theory[47] implemented in the Quantum-ESPRESSO package. The lattice constants of the FCC and HCP Pd and PdH crystals were varied until the optimized lattice parameters were obtained (Extended Data Table 1). The inclusion of the zero-point energy via phonon calculation (Extended Data Fig. 9) is critical for properly comparing the relative stabilities of octahedral vs. tetrahedral occupations of H atoms in Pd interstitial sites[46,48].

To understand the surface effect in a PdH_x nanoparticle, a 2D slab model, infinite in the a–b plane and finite along the c axis, was employed because the full description of a 3D nanoparticle is computationally demanding. To suppress the interaction between periodic images along the c axis, a vacuum region of at least 8 Å was inserted. Owing to the symmetric arrangement of the atoms, no net dipole moment developed, and the error caused by the periodic images was minimal. The energy changes upon the layer-by-layer growth of the FCC and HCP PdH slabs were compared (Extended Data Fig. 5). Alternating Pd and H layers were added, and the formation energy was calculated with respect to FCC Pd and H_2.

Monte Carlo (MC) simulation using embedded atom method (EAM) potential model. The stability of bulk PdH_x crystals with different crystal packing was analyzed using the classical interatomic potential for Pd–H based on the embedded atom method (EAM), which predicts the lattice constants and elastic properties of PdH_x[14]. The total energy of the bulk PdH_x crystals was calculated using the EAM potential at the DFT-optimized geometry for HCP/FCC PdH_x. The DFT-optimized lattice constants were scaled to match the experiments. The H atoms were placed exactly at the octahedral (O) or tetrahedral (T) interstitial sites of the Pd atom unit cells. For the T occupation, H atoms in the equivalenced PdH crystal would fill half of all tetrahedral sites, which were modelled as zinc-blende and wurtzite structures for FCC PdH and HCP PdH, respectively.

An MC simulation of finite-sized PdH nanoparticles was performed to understand the effects of particle size and crystal packing on the relative thermodynamic stability and the internal structure of the nanoparticles. The radii of the nanoparticles were varied from 6 to 30 Å, wherein the Pd atoms were prepared with two different crystal packing (FCC/HCP). The Pd atoms in the FCC/HCP nanoparticles were positioned with ideal FCC and HCC packing using the lattice constants of FCC/HCP PdH obtained from DFT calculations (with scaling to match the experimental lattice constant). The lattice constant of partially hydrogenated PdH_x was obtained by linearly scaling the lattice constants of PdH and pure Pd crystals with FCC/HCP packing. In addition, MC simulations were performed to construct a local H concentration map in the experimentally obtained HCP PdH nanoparticle, which used the 3D atomic coordinates of Pd atoms obtained from the AET experiment.

Each MC move involved the random displacement of H atoms in the fixed Pd nanocrystals. Initially, all H atoms were randomly placed inside the nanoparticles. Each new H atom position was accepted or rejected via Metropolis criteria in the NVT ensemble, where the system temperature was set at 300 K. To ensure that H atoms remained in the nanoparticle, new H positions that were not within a cut-off distance of 2.5 Å from any Pd atoms were rejected. The total energy of the system was equilibrated after a half million accepted MC moves for the smallest nanoparticles. Each nanoparticle was simulated until 5 million MC moves were accepted. The trajectory of the H atom positions was saved for every 100 successful MC moves. The total energy of the nanoparticles and the H occupancy at different interstitial sites (Fig. 2, Extended Data Figs. 2, 7b) was statistically analyzed by averaging the last 1,000 snapshots from each simulation trajectory.

31 Lim, B., Xiong, Y. & Xia, Y. A water-based synthesis of octahedral, decahedral, and icosahedral Pd nanocrystals. *Angew. Chem. Int. Ed.* **46**, 9279-9282 (2007).

32 Buxton, G. V., Greenstock, C. L., Helman, W. P. & Ross, A. B. Critical review of rate constants for reactions of hydrated electrons, hydrogen atoms and hydroxyl radicals (·OH/·O^-) in aqueous solution. *J. Phys. Chem. Ref. Data* **17**, 513-886 (1988).

33 Jung, H. J. *et al.* Spatial variation of available electronic excitations within individual quantum dots. *Nano Lett.* **13**, 716-721 (2013).

34 Duroy, H. & Fourquet, J. Ab-initio structure determination of $LiSbWO_6$ by x-ray powder diffraction. *Mat. Res. Bull.* **23**, 447-452 (1988).

35 AXS, B. Topas v5: General profile and structure analysis software for powder diffraction data.-user's manual. *Karlsruhe, Germany* (2014).

36 Hammond, C. *The basics of crystallography and diffraction*. Vol. 214 (Oxford, 2001).

37 Tian, X. *et al.* Correlating 3D atomic defects and electronic properties of 2D transition metal dichalcogenides with picometer precision. *Bull. Am. Phys. Soc.* (2020).

38 Scott, M. C. *et al.* Electron tomography at 2.4-ångström resolution. *Nature* **483**, 444-447 (2012).

39 Chen, C. C. *et al.* Three-dimensional imaging of dislocations in a nanoparticle at atomic resolution. *Nature* **496**, 74-77 (2013).

40 Pryor, A., Jr. *et al.* GENFIRE: a generalized Fourier iterative reconstruction algorithm for high-resolution 3D imaging. *Sci. Rep.* **7**, 10409 (2017).

41 Giannozzi, P. *et al.* QUANTUM ESPRESSO: a modular and open-source software project for quantum simulations of materials. *J. Phys.: Condens. Matter* **21**, 395502 (2009).

42 Giannozzi, P. *et al.* Advanced capabilities for materials modelling with QUANTUM ESPRESSO. *J. Phys.: Condens. Matter* **29**, 465901 (2017).

43 Perdew, J. P. *et al.* Restoring the density-gradient expansion for exchange in solids and surfaces. *Phys. Rev. Lett.* **100**, 136406 (2008).

44 Blöchl, P. E. Projector augmented-wave method. *Phys. Rev. B* **50**, 17953-17979 (1994).

45 Dal Corso, A. Pseudopotentials periodic table: From H to Pu. *Comput. Mater. Sci.* **95**, 337-350 (2014).

46 Houari, A., Matar, S. F. & Eyert, V. Electronic structure and crystal phase stability of palladium hydrides. *J. Appl. Phys.* **116**, 173706 (2014).

47 Baroni, S., de Gironcoli, S., Dal Corso, A. & Giannozzi, P. Phonons and related crystal properties from density-functional perturbation theory. *Rev. Mod. Phys.* **73**, 515-562 (2001).

48 Long, D. *et al.* Accounting for the thermo-stability of PdH_x (x = 1–3) by density functional theory. *Int. J. Hydrogen Energy* **43**, 18372-18381 (2018).

Declarations

Acknowledgements

This research was supported by the National Research Foundation (grant Nos. 2018M3D1A1058793, 2015M1A2A2074688, 2018M1A2A2061975, 2019R1A2B5B03004854, 2019R1F1A1058236, 2020R1C1C1006239, 2020R1F1A1060331), the Korea Institute of Science and Technology (grant No. 2E30201), and the KAIST-funded Global Singularity Research Program (M3I3).

Author contributions

J.H., J.-H.B., S.J.Y., and D.W.C. conceived the research. J.H. and J.-H.B. designed and performed the experiments, and analyzed the results. H.J. and Y.Y. conducted the atomic electron tomography. H.-Y.P. and S.L. contributed to the synthesis and analysis of nanoparticles. S.J.H., H.C., B.H., and Y.-S.L. carried out the DFT calculations and analysis. C.Y.S. performed the MC calculations and analysis. M.K.C., J.K., and H.B. performed the TEM and EELS acquisition and analysis, while S.-C.K. performed the Rietveld refinement analysis. J.K., Y.S., T.H., and J.P. interpreted the dynamics of nanoparticles in liquids. J.-P.A. and G.H.K. discussed and commented on the results. J.H., J.-H.B., H.J., C.Y.S., Y.Y., Y.-S.L., S.J.Y., and D.W.C. wrote the manuscript. C.Y.S., Y.Y., Y.-S.L., S.J.Y., and D.W.C. supervised the project. All authors approved the final version of the manuscript for submission.

Competing interests

The authors declare no competing interests.

Figures

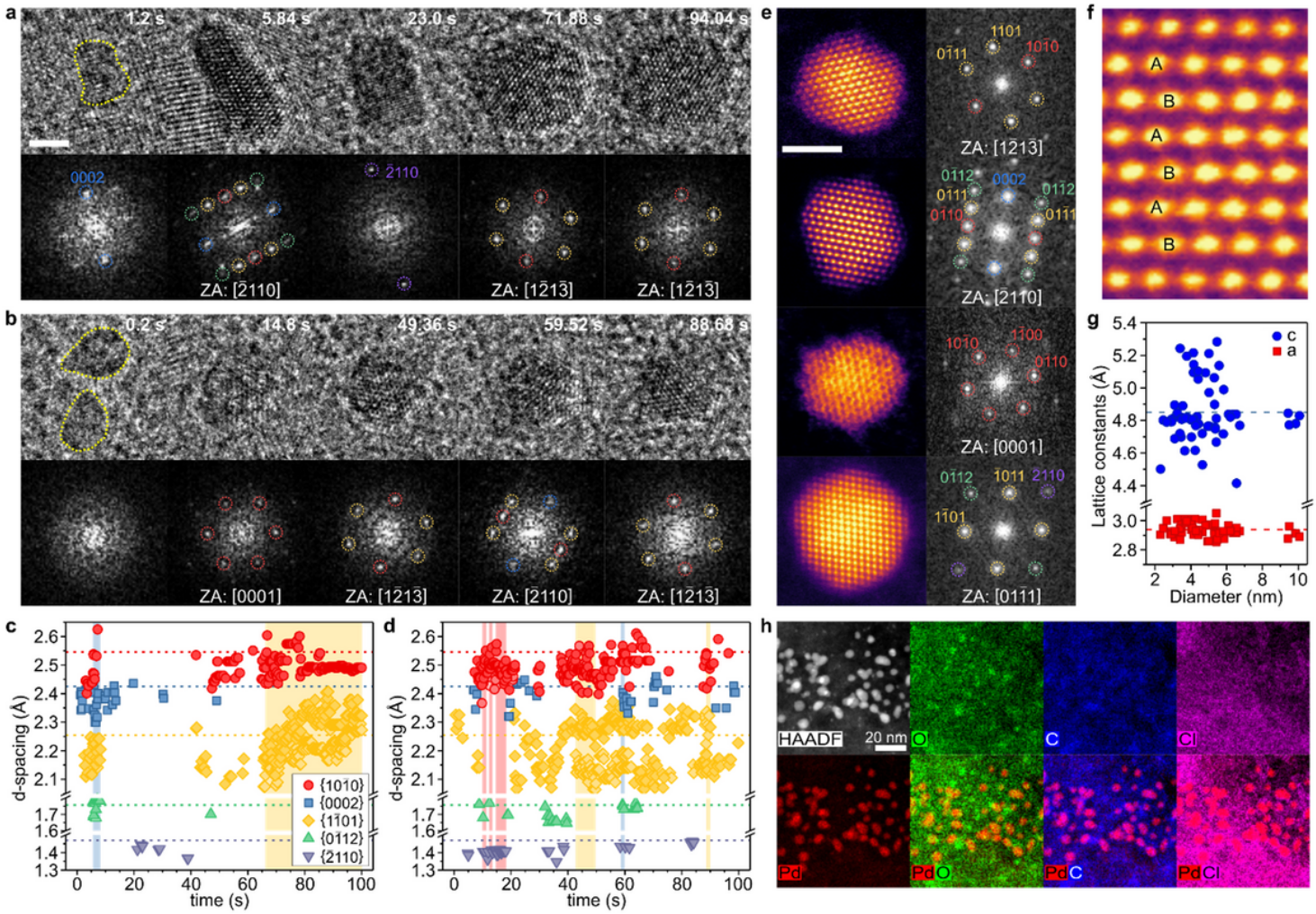


Figure 1

In situ and ex situ TEM analysis of HCP Pd nanoparticles in a GLC. a–b, Snapshots from movies S1 and S2 of Pd nanoparticle growth and corresponding FFTs, with the growth occurring via (a) monomer attachment (particle 1) and (b) coalescence (particle 2) in GLC under an electron dose rate of 1.0 × 104 e-/Å2s. Every zone axis (ZA) pattern matched with that of HCP lattice, while lattice fringes around the nanoparticle resulted from a 2D NaCl crystal. c–d, Temporal changes in interplanar distance of five low-index planes in particles (c) 1 and (d) 2. Blue-, yellow-, and red-shaded boxes in (c) and (d): time span when the particle was aligned along the [-2110], [1-21-3], and [0001] zone axes of HCP, respectively. Horizontal dashed lines: mean d-spacings of each crystallographic plane obtained from ex situ measurements. e, HR-STEM images and FFTs of four different particles, which were found to be consistent with [1-21-3], [-2110], [0001], and [01-11] ZA patterns of HCP lattice. Dashed circles: low-index planes colored according to each family of planes. f, ABAB stacking of Pd atoms observed in the particle along the [-2110] ZA in (e). g, Lattice constants of HCP particles formed in GLC under a dose rate >5.0 × 102 e-/Å2s as a function of particle size, showing no correlation. Dashed lines: average values of a = 2.94 Å (red) and c = 4.85 Å (blue). h, EDS map of the nanoparticles indicating they are composed of only Pd. Scale bars, 2 nm unless stated otherwise.

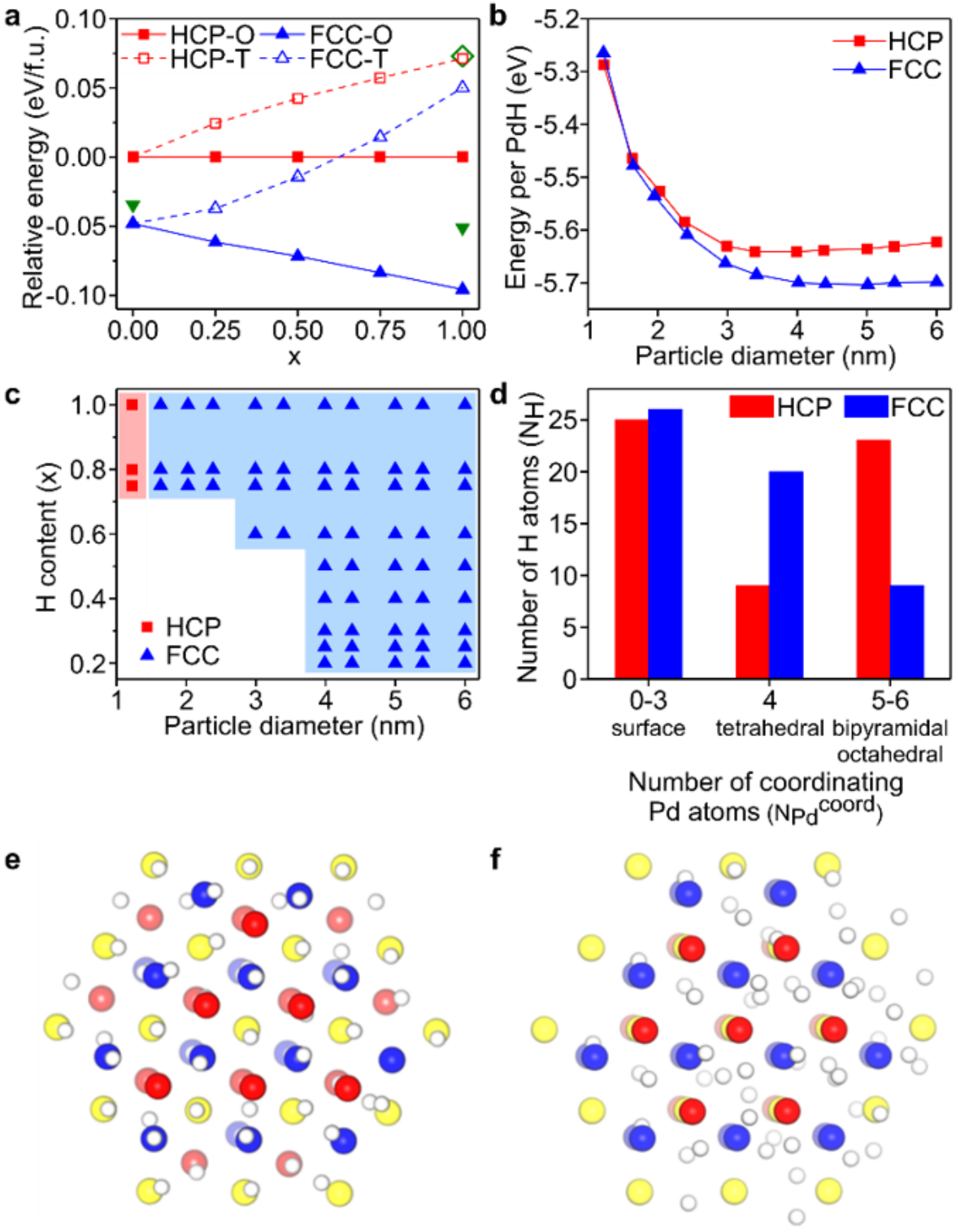


Figure 2

Thermodynamic stability of FCC/HCP PdHx nanoparticles predicted by simulations. a, Comparison of total energy per formula unit (E) for various PdHx bulk periodic crystals. Energies calculated with embedded atom method (EAM) potentials are represented as blue triangles and red squares (lines connecting the data points are visual guides) for FCC and HCP crystal packing, respectively. Solid lines/filled symbols and dashed lines/empty symbols: octahedral (O) and tetrahedral (T) positional

occupation of H, respectively, with energy of HCP-O for reference. The green-filled inverse triangle and the green-outlined empty diamond represent the energy difference between FCC-O/HCP-O and HCP-T/HCP-O, respectively, including the zero-point vibrational energy obtained from DFT calculations. b, MC-simulated thermodynamic stability of equivalenced PdH nanoparticles with different particle sizes and crystal packing. Pd atoms are fixed at DFT-optimized positions with either FCC or HCP packing, while H atoms are allowed to move freely until the energy and structure are equilibrated at the ambient conditions. c, Phase diagram of finite-sized PdHx nanoparticles with different particle diameters and H contents (x). The uncategorized area for small nanoparticles with low H contents represents the region where FCC and HCP packing show very similar energies. d, Partitioning of H atoms (white small spheres in (e) and (f)) and e–f, snapshots of equilibrated structures obtained from MC simulations for sub-nanometer (12 Å) PdH nanoparticles. The positions of the Pd atoms (large spheres with colors representing different layers) are fixed in the (e) FCC and (f) HCP crystal lattices. Each nanoparticle contains five Pd layers with (e) ABCA'B' and (f) ABA'B'A" packing. Owing to the small number of layers, nearly half of the H atoms are located in the surface region (NPdcoord = 0–3), and the extra stabilization by the 1-4 AA' overlap is lost in many FCC-O sites, thus reducing the stability of FCC-O sites in this small nanoparticle. Unlike the bulk periodic crystal, more internal H atoms in the FCC nanoparticle occupy T sites than O sites.

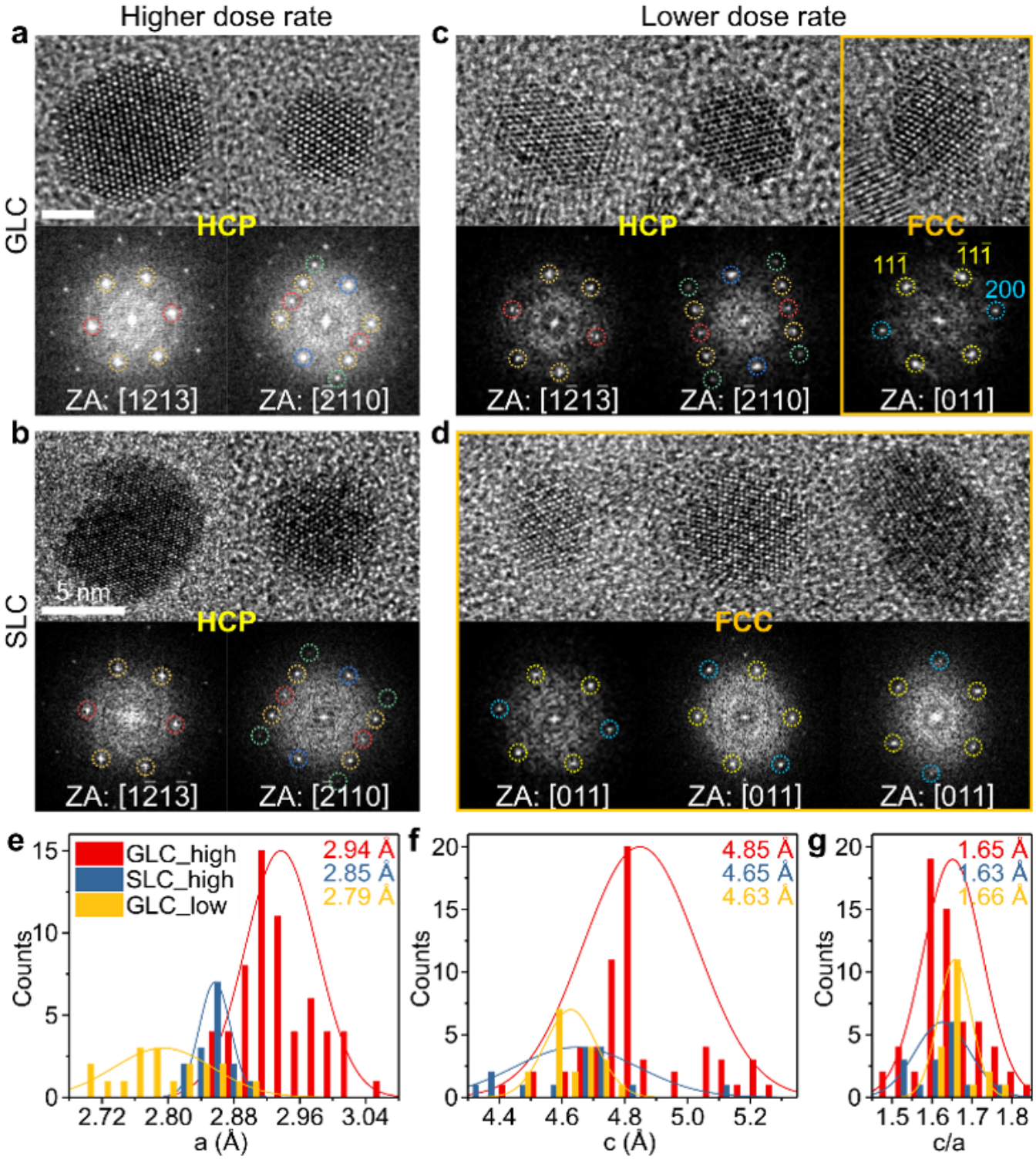


Figure 3

Dependence of nanoparticle structure on electron dose rate and liquid cell type. a–d, HR-TEM images and corresponding FFTs of particles formed under dose rates between 5.0 × 102 e-/Å2s and 1.0 × 104 e-/Å2s (higher dose rate) in (a) GLC and (b) Si3N4 liquid cell (SLC), and under dose rates between 0.6 e-/Å2s and 5.0 × 101 e-/Å2s (lower dose rate) in (c) GLC and (d) SLC. The volumes of most FCC nanoparticles were not greater than those of pure Pd nanoparticles. Scale bars, 2 nm unless stated otherwise. ZA, zone axis.

e–g, Histograms of lattice constants a, c, and c/a of HCP particles formed in GLC and SLC under two different dose rate ranges: higher dose rate in GLC (red, GLC_high) and SLC (blue, SLC_high), and lower dose rate in GLC (yellow, GLC_low). Average values for each case appear in the top right of each plot. Standard deviations of the values for GLC_high, SLC_high, and GLC_low experiments are (e) 0.04, 0.02, and 0.06 Å for a, (f) 0.18, 0.20, and 0.08 Å for c, and (g) 0.07, 0.07, and 0.04 Å for c/a, respectively. Unlike the c/a value, a and c of GLC_high are greater than those of SLC_high and GLC_low.

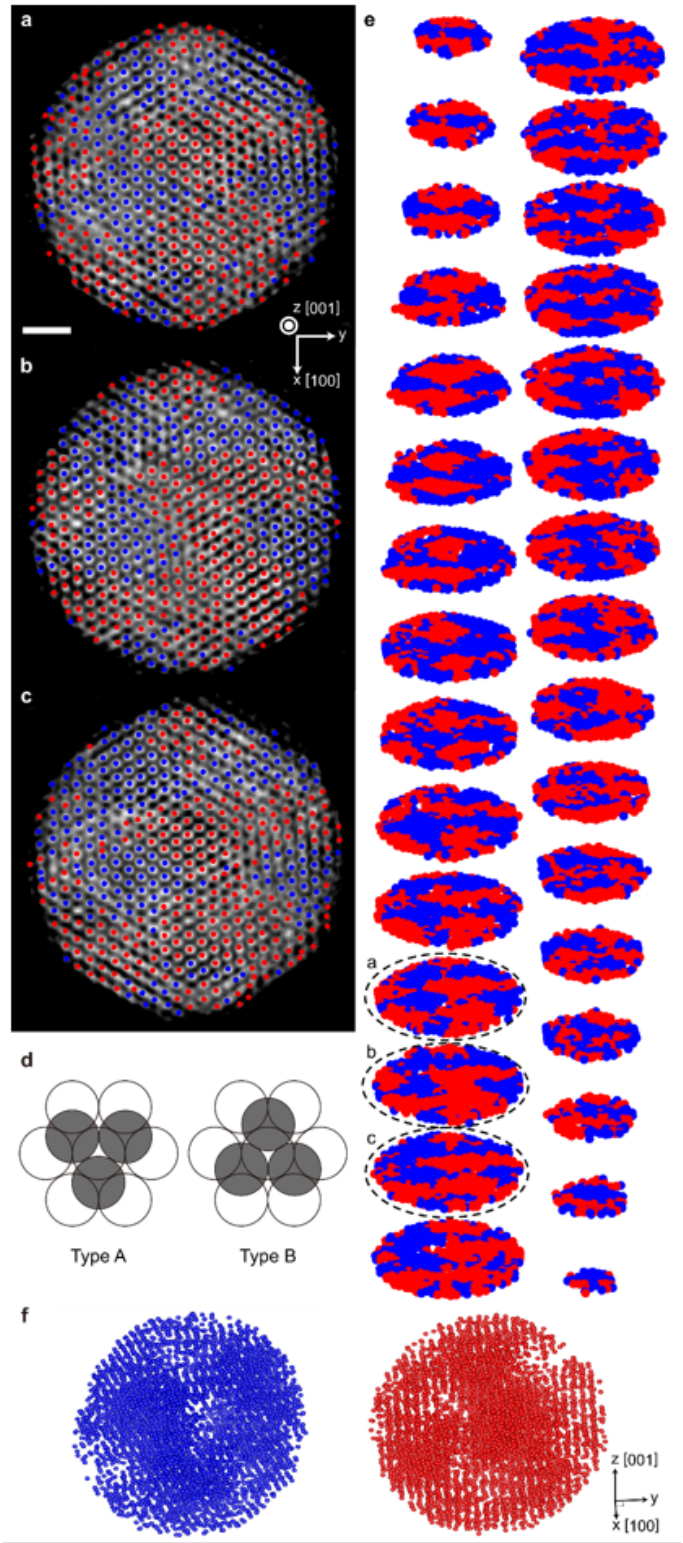


Figure 4

Three-dimensional single-atom-level structural analysis of a PdHx nanoparticle. a–c, Reconstruction intensity and traced atomic coordinates of three consecutive atomic layers of a nanoparticle. Grayscale background represents the sliced intensity of the reconstructed 3D tomogram, and blue and red dots represent the positions of traced atoms belonging to ABAB and BABA stacking, respectively. Interlayer atoms (which do not clearly belong to one of the HCP atomic layers) are plotted in the layers which best represent their in-plane positions. Scale bar, 1 nm. d, Schematic diagram of the two different types (type A and B) of nearest-neighbor arrangements in an HCP crystal. e, Hexagonal stacking types revealed by 3D atomic structural analysis via AET. Each slice represents an atomic layer of the nanoparticle perpendicular to the hexagonal c axis, where ABAB-type and BABA-type regions are colored blue and red, respectively. Layers corresponding to those in (a–c) are marked with black dashed lines. f, 3D atomic structures separately drawn for atoms of each stacking type. ABAB-type and BABA-type atoms are blue and red, respectively.

Supplementary Files

This is a list of supplementary files associated with this preprint. Click to download.

- ExtendedData.docx
- FinalSupplementaryInformation.docx
- MovieS1Final.mp4
- MovieS2Final.mp4
- MovieS3Final.mp4